nature communications

Article

https://doi.org/10.1038/s41467-025-56339-2

Silver single atoms and nanoparticles on floatable monolithic photocatalysts for synergistic solar water disinfection

Received: 24 July 2024

Accepted: 16 January 2025

Jian Wang [1], **Jiahe Zhang** [2], **Yang Li** [1] ✉, **Xinghui Xia** [1], **Hengjing Yang** [1], **Jae-Hong Kim** [3,4] & **Wen Zhang** [2]

Photocatalytic water disinfection technology is highly promising in off-grid areas due to abundant year-round solar irradiance. However, the practical use of powdered photocatalysts is impeded by limited recovery and inefficient inactivation of stress-resistant bacteria in oligotrophic surface water. Here we prepare a floatable monolithic photocatalyst with ZIF-8-NH_2 loaded Ag single atoms and nanoparticles (Ag_{SA+NP}/ZIF). Atomically dispersed Ag sites form an Ag−N charge bridge, extending the lifetime of charge carriers and thereby promoting reactive oxygen species (ROS) generation. The photothermal effect of the plasmonic Ag nanoparticles reduces the bacterial resistance to ROS and impairs DNA repair capabilities. Under sunlight irradiation, the synergistic effect of Ag single atoms and nanoparticles enables 4.0 cm^2 Ag_{SA+NP}/ZIF to achieve over 6.0 log inactivation (99.9999%) for the stress-resistant *Escherichia coli* (*E. coli*) in oligotrophic surface water within 30 min. Furthermore, 36 cm^2 Ag_{SA+NP}/ZIF is capable of disinfecting at least 10.0 L of surface water, which meets the World Health Organization (WHO) recommended daily per capita drinking water allocation (8.0 L). This study presents a decentralized and sustainable approach for water disinfection in off-grid areas.

Water pollution caused by pathogenic microorganisms poses a serious threat to public health. Millions of individuals in developing nations succumb to mortality each year due to the consumption of water contaminated with pathogenic microorganisms[1,2]. Every 2 min a child under the age of five perishes from diarrheal diseases caused by poor sanitation and substandard water quality[3,4]. Since the 20th century, the implementation of urban water supply network systems and centralized water treatment facilities has significantly mitigated infections caused by waterborne pathogens. However, effective access to safe drinking water remains scarce in off-grid rural areas, such as in sub-Saharan Africa, North Africa, and the Middle East[5], often due to lack of electricity and other vital water treatment infrastructures to ensure reliable and safe drinking water access. With the intensification of climate change, it is estimated that 3.6 billion people worldwide currently live in regions that may face potential water scarcity, and this number could rise to 5.7 billion by 2050[6]. Therefore, improving water management and sanitation is critical for communities that have no or limited access to traditional water disinfection methods.

Point-of-use (POU) disinfection at household or community scale is one of the most promising solutions in addressing this issue[5,7]. POU disinfection technologies eliminate the need for expensive large-scale water treatment equipment and avoid the complexities associated with transportation and storage procedures. Despite decades of technological advances, existing POU disinfection technologies still face issues with high energy consumption (e.g., boiling water), generation of carcinogenic by-products (e.g., chlorination), and high costs

---

[1] Key Laboratory of Water and Sediment Sciences of Ministry of Education & State Key Laboratory of Water Environment Simulation, School of Environment, Beijing Normal University, Beijing 100875, China. [2] Department of Civil and Environmental Engineering, New Jersey Institute of Technology, Newark, NJ 07102, USA. [3] Department of Chemical and Environmental Engineering, Yale University, New Haven, CT 06511, USA. [4] School of Civil, Environmental and Architectural Engineering, Korea University, 145 Anam-ro, Seongbuk-gu, Seoul 02841, Republic of Korea. ✉e-mail: liyang_bnu@bnu.edu.cn

(e.g., reverse osmosis)[8–10]. Fortunately, among the 64 countries with <80% rural access to basic drinking water services, solar irradiance (5.59 kWh m^{-2} per day) significantly exceeds the global average (4.70 kWh m^{-2} per day)[5], offering valuable opportunities for solar energy-driven water treatment. Therefore, the development of advanced materials and processes that can fully harness solar energy to inactivate microorganisms will contribute to the attainment of environmentally friendly and sustainable water disinfection in off-grid communities.

Single-atom photocatalysts (SAPCs) have been reported for disinfection due to their maximum metal atom utilization and efficient charge separation[11–13]. SAPCs are known to generate ROS that attack cell membranes and intracellular components like DNA[14]. However, microorganisms possess innate damage repair system, such as DNA repair process (SOS response), which confer resistance to ROS stresses[15]. Such resistance is more pronounced in microorganisms at late stationary phase in natural waters[16–18]. In oligotrophic surface water, bacteria at this growth phase are usually starved, and their adaptation to starvation enhances their tolerance to ROS and other environmental stresses[19]. This is why these bacteria cultured under above specific conditions are usually called stress-resistant bacteria. Consequently, numerous photocatalysts exhibiting exceptional antimicrobial performance in laboratory show limited bactericidal effectiveness in real water environments, posing challenges for their large-scale applications. Nanoparticles with plasmonic effects, such as Ag and Au, exhibit excellent photothermal properties through collective resonance of free charge carriers and non-radiative decay processes[20,21]. Previous studies have shown that photothermal ablation can target tumor cell proteins and promote protein aggregation, consequently interfering with DNA damage repair[22]. Given that the bacterial inactivation by SAPCs relies on ROS-mediated intracellular DNA damage, any potential reduction in bacterial DNA repair capacity due to the photothermal effect would significantly enhance the bactericidal efficiency. Hence, we speculate that SAPCs integrated with plasmonic nanoparticles could effectively inactivate stress-resistant microorganisms in water.

In the synthesis of SAPCs, the prevalent use of powdered supports such as carbon nitride and metal oxide materials to anchor single atoms may interfere their recovery in aqueous reactions[23–25], thereby increasing the contamination risk throughout the disinfection process[16]. In addition, the widespread presence of suspended sediment and natural organic matter in the natural water significantly interferes with the light absorbance of SAPCs[5]. To improve catalyst recovery and light absorption, previous studies have employed polymer binders to immobilize catalysts on the platforms such as nickel foam and ceramic plate[26,27], resulting in compromised accessibility of the potential active reaction sites and hindered electron transfer[28–30]. Consequently, there is an urgent need to avoid using polymer binders while strengthening the stability of the catalytic layer on the support. This requirement can be effectively fulfilled by the fabrication of binder-free floatable monolithic photocatalysts via loading metal cocatalysts into the floatable monolithic supports.

Here, we prepared a silver single-atom and nanoparticle-loaded floatable monolithic photocatalyst (Ag_{SA+NP}/ZIF) via a two-step synthesis method as shown in Fig. 1a. Firstly, a monolithic metal-organic frameworks ZIF-8-NH_2 layer was synthesized in situ by a ligand evaporation deposition strategy, employing 3D melamine sponges with zinc ions as a substrate, and utilizing 2-methylimidazole and 2-aminobenzimidazole as organic ligands. ZIF-8-NH_2 material possesses semiconducting properties and is frequently employed as support for loading metal cocatalysts[31,32]. Abundant N atoms with lone pair of electrons in ZIF-8-NH_2 can form strong coordination with Ag metal atoms, effectively preventing their migration and aggregation[23,33]. The low density of sponges ensures that the monolithic photocatalyst can float on water. The monolithic photocatalyst was selectively loaded with Ag_{SA} and Ag_{NP} using the ice-photoreduction method, wherein the photocatalytic reaction primarily occurs on the submerged surface with sunlight exposure (Fig. 1b). Ag_{SA+NP}/ZIF can be utilized in a tablet-like form for convenient recyclable water disinfection. Under natural light irradiation, the photothermal effect of Ag_{SA+NP}/ZIF synergizes with photogenerated ROS to inactivate stress-resistant bacteria in oligotrophic surface water. This monolithic photocatalyst exhibits practical advantages for POU water disinfection, as evidenced by its performance, recyclability, durability, and cost-effectiveness validated in this study.

Results

Material characterization

The photocatalyst support consists of a 3D melamine sponge and ZIF-8-NH_2 layer. As shown in Fig. 2a, a dense and continuous ZIF-8-NH_2 layer was deposited on the surface of the melamine sponge. The thickness of ZIF-8-NH_2 coating is 1.0-1.4 µm. Cross-sectional scanning electron microscope (SEM) image (Supplementary Fig. 1) shows that some ZIF-8-NH_2 crystals were infused into the inner sponge layer, which potentially enhances the adhesion between the surface ZIF-8-NH_2 layer and substrate. X-ray diffraction (XRD) patterns verified that the surface layer exhibits intact ZIF-8-NH_2 crystal structure (Supplementary Fig. 2)[34]. Transmission electron microscopy (TEM) images show successful loading of Ag nanoparticles with an average size of 13.1 nm (Fig. 2b and Supplementary Fig. 3).

Aberration-corrected high-angle-annular-dark-field scanning transmission electron microscopy (AC-HAADF-STEM) images (Fig. 2c and Supplementary Fig. 4) show atomically dispersed Ag (circled bright spots). The elemental mapping images also confirm that Ag atoms and nanoparticles dispersed on ZIF-8-NH_2 (Fig. 2d). Thus, Ag single atoms and nanoparticles were both present on this monolithic photocatalyst. The total Ag loading content was 1.28 wt% as detected by an inductively coupled plasma optical emission spectrometer (ICP-OES), where the proportion of Ag single atoms and Ag nanoparticles was 46.9% and 53.1%, respectively. In addition, the 1.21 wt% Ag single-atom-loaded ZIF-8-NH_2 (Ag_{SA}/ZIF) and 1.16 wt% Ag nanoparticle-loaded ZIF-8-NH_2 (Ag_{NP}/ZIF) were also prepared for comparative studies and their AC-HAADF-STEM and TEM images are shown in Supplementary Fig. 5.

A measurement of X-ray absorption fine structure (XAFS) was carried out to further investigate the dispersion and coordination environment of Ag species[35]. Fourier-transformed (FT) extended Ag K-edge X-ray absorption fine structure (EXAFS) spectra show that Ag_{SA}/ZIF and Ag_{SA+NP}/ZIF share a common peak at 1.56 Å, which may be attributed to the coordination of Ag single atoms with N or C (Fig. 2e). The best-fitting result for EXAFS spectrum of Ag_{SA+NP}/ZIF shows that the dominant peak at 1.56 Å can be attributed to the Ag−N coordination (Fig. 2f and Supplementary Table 1). The Ag−N and Ag−Ag coordination numbers are 1.5 and 4.6 at bond distances of 2.02 Å and 2.83 Å, respectively. In addition, a peak at 2.7 Å was observed in both Ag_{SA+NP}/ZIF and Ag_{NP}/ZIF, resembling the characteristic Ag−Ag peak of metallic Ag, thereby confirming the presence of Ag nanoparticles in these samples.

Optical and photothermal properties

Light capture and photogenerated carrier separation play key roles in photocatalytic disinfection reactions[16,36]. As shown in Fig. 3a, compared to ZIF-8-NH_2, Ag_{SA+NP}/ZIF exhibits the strongest light absorption in the visible region, which may result from the introduction of Ag single atoms and nanoparticles[37,38]. The light absorption intensity of Ag_{NP}/ZIF is higher than that of Ag_{SA}/ZIF, indicating a more significant contribution from the plasmonic Ag nanoparticles to light adsorption capacity. The noise at 300-380 nm originates from the sponge (Supplementary Fig. 6a). The plasmonic peak of Ag nanoparticles is absent at 450 nm, probably due to the low Ag loading (1.16 wt% for Ag_{NP}/ZIF)

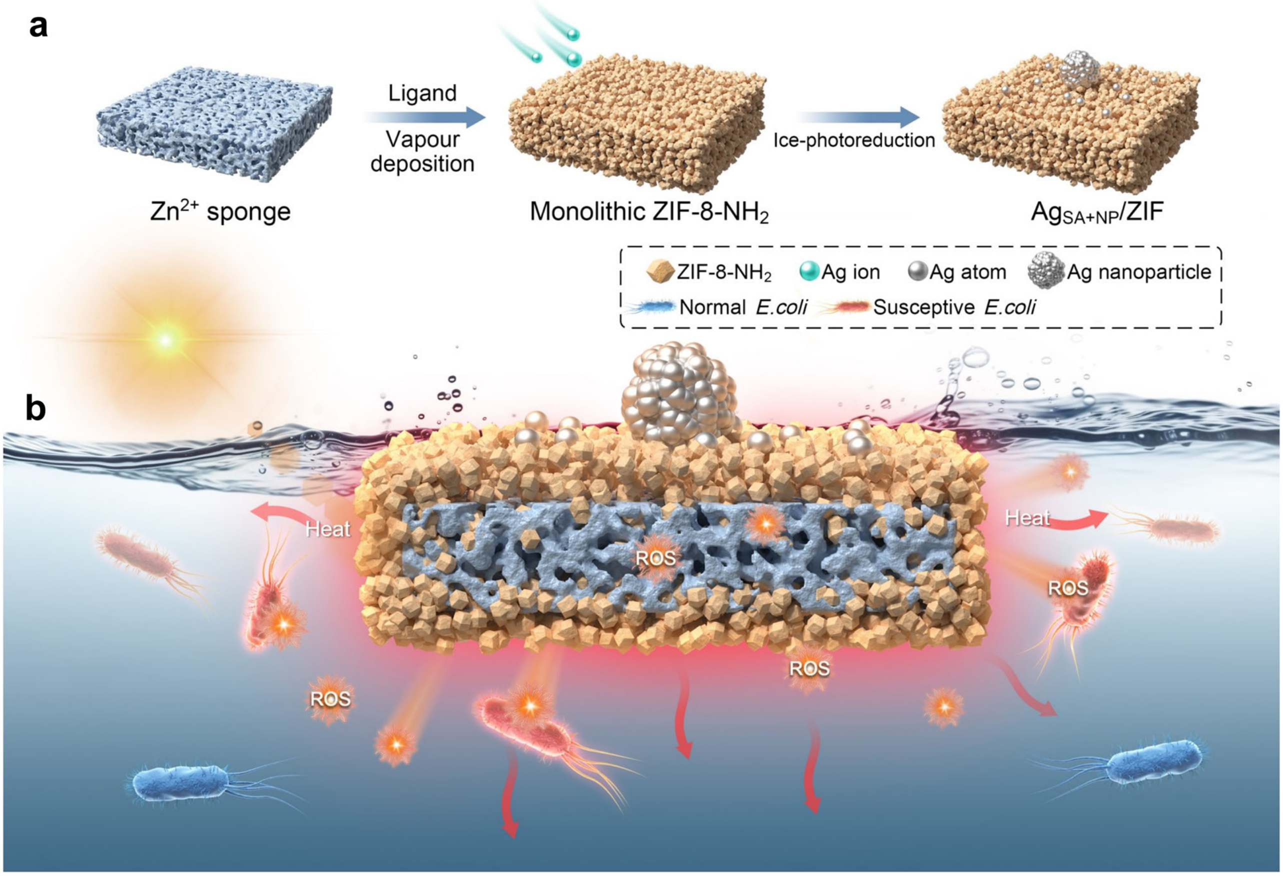

Fig. 1 | Overview of the floatable monolithic photocatalyst. **a** Synthesis schematic of Ag_{SA+NP}/ZIF. **b** Disinfection operation schematic of Ag_{SA+NP}/ZIF. Note that Ag species are magnified in size.

and the overlaps of the significant optical absorption of ZIF-8-NH_2 with the weak plasmonic peak[39].

The increased light absorption by Ag nanoparticles can be attributed to the local electromagnetic enhancement resulting from the localized surface plasmon resonance[40]. Noble metal (e.g., gold and silver) nanoparticles contain large numbers of freely mobile electrons that can strongly interact with light by either absorbing or scattering photons[20,21]. The oscillating electric field of the incoming radiation induces coherent collective oscillation of the free electrons on the metal surface[20,21]. Supplementary Fig. 6b shows the simulation of the electromagnetic field at the interface between one single Ag nanoparticle (e.g., 13 nm in diameter) and ZIF-8-NH_2 under 450 nm irradiation using COMSOL Multiphysics. The average enhancement factor, defined as $P = |E|/E_O$, quantifies the amplification of the localized electric field (E) after light irradiation relative to the electric field (E_O) before light irradiation in the near-field region of the Ag nanoparticle. Clearly, along the distance from the core of the Ag nanoparticle, the local electromagnetic field yielded a P-value of >10-fold due to the dynamic charge accumulation at the Ag nanoparticle surface under a 450 nm planewave excitation. In addition, the effects of ZIF-8-NH_2 thickness and Ag nanoparticle size on the electromagnetic field enhancement are evident. The results presented in Fig. 3b demonstrate a proportional increase in the enhancement factor as the radius of Ag nanoparticles ranges from 1.0 to 8.0 nm. It is observed that the thickness of ZIF-8-NH_2 does not significantly impact the enhancement factor when exceeding 4.0 nm. Furthermore, there is no enhancement of the electric field intensity within the near field of pure ZIF-8-NH_2 (Supplementary Fig. 6c), suggesting that the interface between ZIF-8-NH_2 substrate and Ag nanoparticle is essential for enhancing the light absorbance of the photocatalyst[22].

Furthermore, the band gap of Ag_{SA+NP}/ZIF was determined to be 2.78 eV, which is smaller than that of pure ZIF-8-NH_2 (3.47 eV) as compared by the Tauc plots in Supplementary Fig. 7a, b. The strong local electric field generated by Ag nanoparticles or the formation of Ag–N coordination might influence the electronic density distribution in ZIF-8-NH_2, consequently modulating its band gap[41,42]. Mott-Schottky plots of Ag_{SA+NP}/ZIF were employed to determine the conduction band minimum (CBM) (Supplementary Fig. 7c). Higher CBM (−0.43 V vs. NHE) of Ag_{SA+NP}/ZIF than reduction potential of O_2 to $O_2^{\bullet-}$(−0.33 V vs. NHE) implies the feasibility of Ag_{SA+NP}/ZIF for ROS generation[43].

The concentration of ROS production depends on the separation of photogenerated carriers, which was investigated by steady-state fluorescence spectroscopy and time-resolved photoluminescence (TRPL) spectroscopy. As shown in Fig. 3c, both Ag_{SA+NP}/ZIF and Ag_{SA}/ZIF exhibited lower fluorescence intensities compared to Ag_{NP}/ZIF, indicating that the recombination of electron-hole pairs was inhibited. This is because the atomically dispersed Ag provides more reactive sites to capture the photogenerated electrons[44]. As shown in Fig. 3d and Supplementary Table 2, the average lifetime of photogenerated charge carriers in Ag_{SA}/ZIF (1.67 ns) exceeds those in Ag_{SA+NP}/ZIF (1.53 ns) and Ag_{NP}/ZIF (1.10 ns). The Ag content of Ag_{SA}/ZIF is 1.21 wt%, which is lower than that of Ag_{SA+NP}/ZIF (1.28 wt%). Nonetheless, Ag_{SA}/ZIF exhibits a longer charge carrier lifetime, indicating that Ag_{SA} is more conducive to the capture of photogenerated electrons. Moreover, Ag_{SA+NP}/ZIF and Ag_{SA}/ZIF show smaller impedance arc radii in electrochemical impedance spectra compared to Ag_{NP}/ZIF (Fig. 3e). The charge transfer resistance (R_{ct}) of Ag_{SA}/ZIF is 25.5 KΩ, which is lower than that of Ag_{SA+NP}/ZIF (39.0 KΩ). The atomically dispersed Ag atoms bonded with N atoms facilitates the formation of Ag–N charge

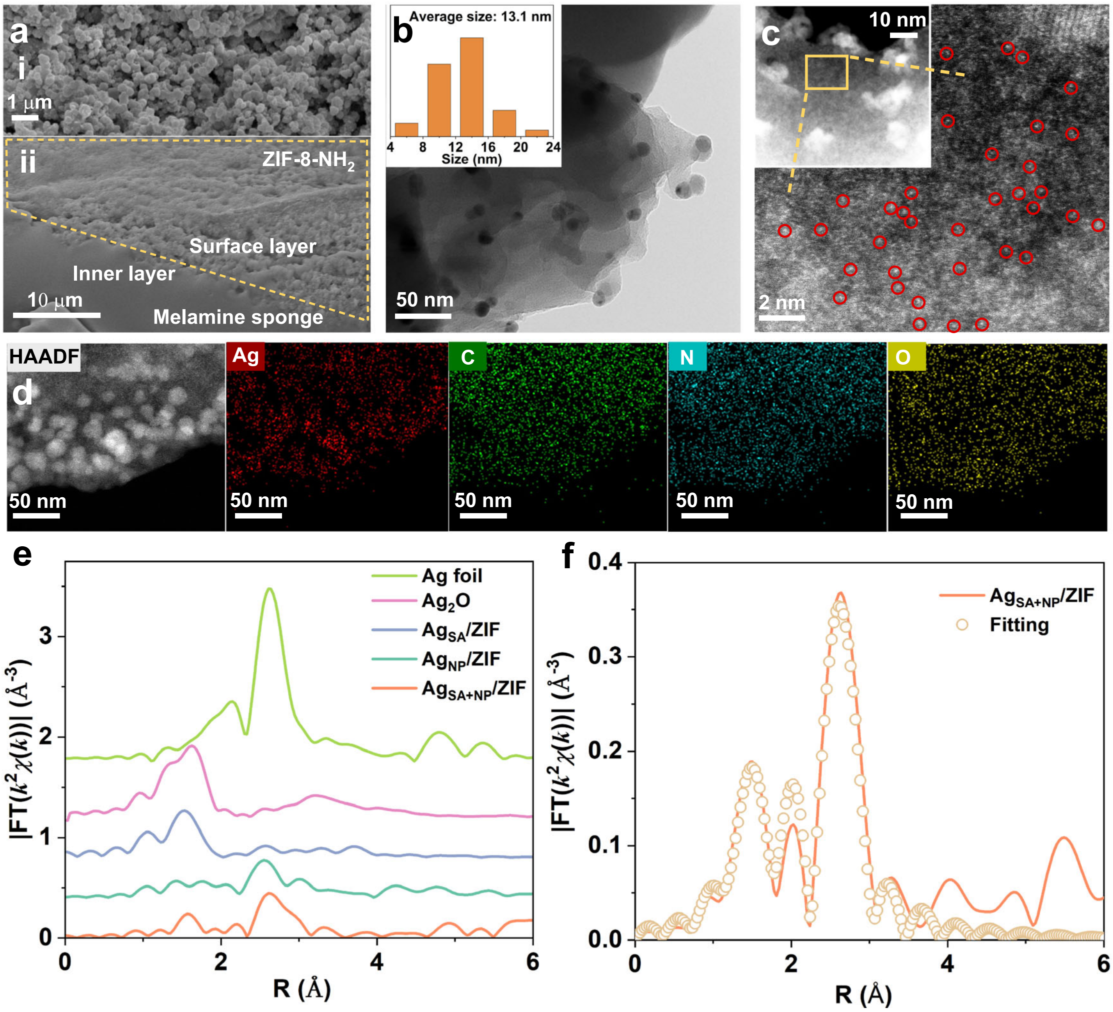

Fig. 2 | Structural characterization of Ag$_{SA+NP}$/ZIF. **a** Top (**i**) and (**ii**) cross-sectional view SEM images of monolithic ZIF-8-NH$_2$ support. **b** TEM image of Ag$_{SA+NP}$/ZIF. Inset is the statistical size distribution of Ag nanoparticles. **c** AC-HAADF-STEM image of Ag$_{SA+NP}$/ZIF (the bright dots in the red circles are Ag single atoms). Inset is the HAAD-STEM image of Ag$_{SA+NP}$/ZIF. **d** HAADF-STEM with elemental mapping images of Ag$_{SA+NP}$/ZIF. **e** Fourier-transformed EXAFS results of Ag$_{SA}$/ZIF, Ag$_{NP}$/ZIF, Ag$_{SA+NP}$/ZIF, Ag foil and Ag$_2$O at the Ag K-edge. **f** EXAFS fitting curve of Ag$_{SA+NP}$/ZIF in R space.

bridge. This configuration significantly enhances the metal-support interaction, thereby boosting the charge transfer[39]. Hence, we conclude that the incorporation of Ag single atoms endows monolithic ZIF-8-NH$_2$ with intensive photochemical properties.

The photothermal properties of the dry monolithic photocatalysts were investigated by infrared thermal imaging. After exposure to simulated visible light (400-760 nm) at an intensity of 100 mW cm^{-2}, the dry surface temperatures of Ag$_{SA+NP}$/ZIF and Ag$_{NP}$/ZIF rapidly increase to 67.1 and 72 °C within 15 min, respectively, followed by a plateau (Fig. 3f, g). In comparison, monolithic ZIF-8-NH$_2$ and Ag$_{SA}$/ZIF demonstrated weak photothermal effects (<36 °C) after 60 min light irradiation. Both Ag$_{SA+NP}$/ZIF and Ag$_{NP}$/ZIF exhibit greater photothermal effects due to surface plasmon resonance of Ag nanoparticles[22]. We further evaluated the water temperature elevation induced by monolithic photocatalysts under natural light irradiation of 33.0-35.0 mW cm^{-2}, which is approximately equivalent to the average daily irradiance (5.59 kWh m^{-2} per day) for most off-grid areas[5]. As shown in Fig. 3h, the utilization of Ag$_{SA+NP}$/ZIF resulted in a significant elevation of water temperature to 41.8 °C within 15 min light irradiation, whereas the ZIF-8-NH$_2$ and Ag$_{SA}$/ZIF-treated group exhibited only a minor increase in water temperature (<36.7 °C). These results indicate that Ag$_{SA+NP}$/ZIF possesses pronounced photothermal heating properties.

Natural water disinfection performance

We investigated the water disinfection performance of Ag$_{SA+NP}$/ZIF toward stress-resistant bacteria *E. coli* at late stationary phase cultivated in the river water from the upper reaches of Yellow River. The chemical parameters of the water are shown in Supplementary Table 3, wherein the total organic carbon (TOC) is 5.49 mg L^{-1} and primarily originates from natural organic matter that exhibits light absorption properties. However, unlike water-dispersed particulate catalysts, Ag$_{SA+NP}$/ZIF floating at the water surface (Fig. 4a) remains unaffected by impurities in the water, thereby ensuring efficient light delivery.

Firstly, we assessed the disinfection activity of different areas of Ag$_{SA+NP}$/ZIF against the stress-resistant *E. coli* in 0.1 L river water under 30 min of 33.0-35.0 mW cm^{-2} solar irradiation (Fig. 4b). Four cm^2 Ag$_{SA+NP}$/ZIF achieved a 6.50 log$_{10}$ reduction of *E. coli*, implying almost complete inactivation of the bacteria. Under a dark condition, a mere 0.44 log$_{10}$ reduction was detected, indicating that the inactivation of bacteria was light-driven, thus ruling out adsorptive removal of bacteria by Ag$_{SA+NP}$/ZIF. The bactericidal activity of the 1 cm^2 and 2 cm^2 Ag$_{SA+NP}$/ZIF exhibited a reduction of at least 4 log$_{10}$ compared to the 4 cm^2 Ag$_{SA+NP}$/ZIF. This decrease can be attributed not only to the lower photocatalyst dosage but also to the inability of the smaller samples to raise the water temperature above 37 °C (Supplementary Fig. 8). In contrast, 4 cm^2 Ag$_{SA+NP}$/ZIF effectively increased the water

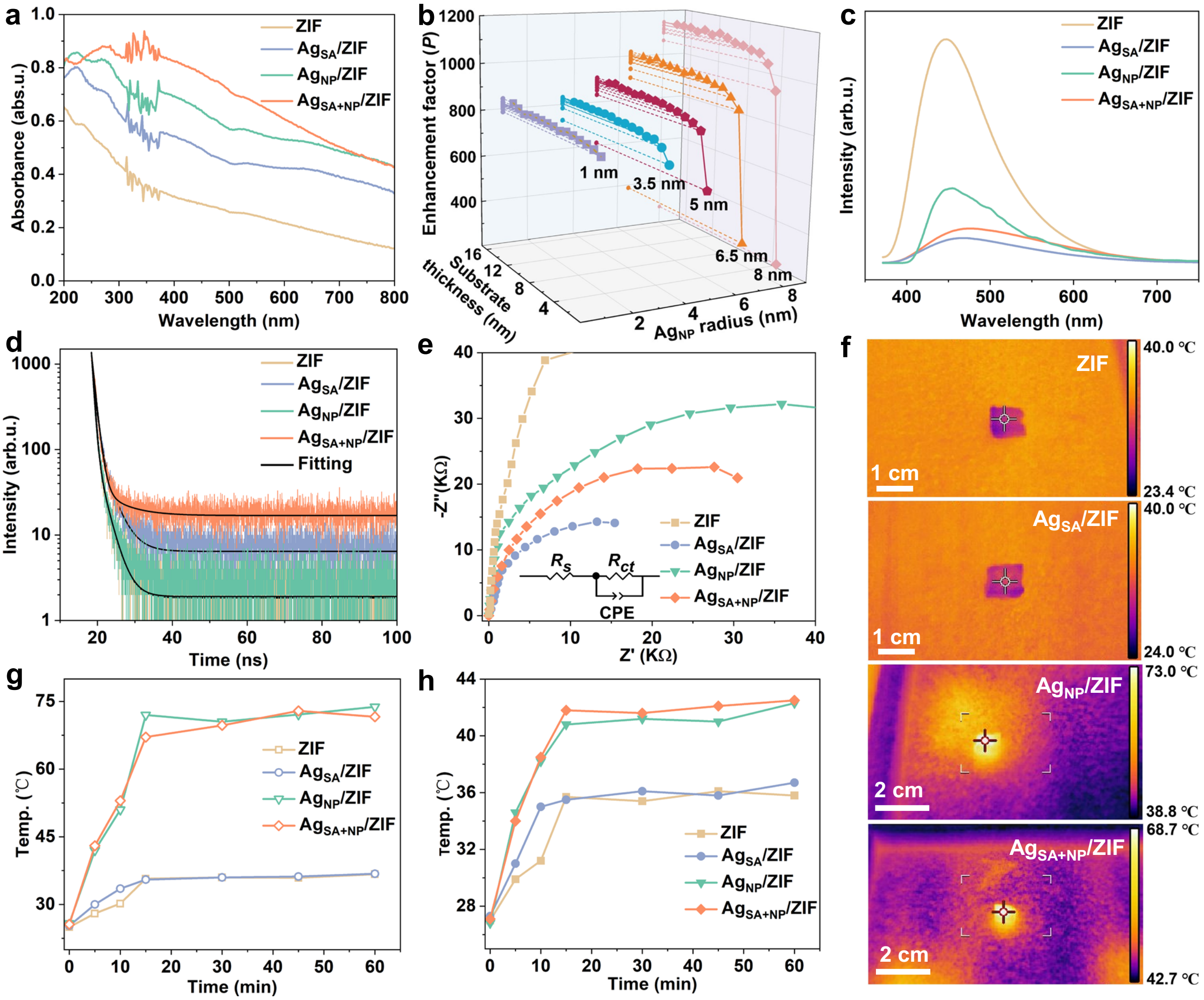

Fig. 3 | Optical and photothermal properties of the photocatalysts. a UV-Vis diffuse reflectance spectra of photocatalysts. **b** Electromagnetic simulations: enhancement factor of electric field on the Ag nanoparticle-ZIF-8-NH$_2$ surface under visible light (450 nm) irradiation. **c**, **d** Steady-state fluorescence spectra (**c**) and TRPL decay curves (**d**) of photocatalysts, the excitation wavelength is 375 nm. **e** Electrochemical impedance spectra of photocatalysts, inset shows the corresponding equivalent circuit diagram. R_s: Solution resistance; CPE: Constant phase element. **f** Infrared thermal images of photocatalysts under simulated visible light (400-760 nm) irradiation at an intensity of 100 mW cm^{-2} for 15 min. **g** Temperature elevation curves of photocatalysts under simulated visible light (400-760 nm) irradiation at an intensity of 100 mW cm^{-2}. **h** Temperature elevation curves of water after adding the monolithic photocatalyst under natural light irradiation. Reaction condition: 2 × 2 cm^2 catalyst; 0.1 L Yellow River water from upper reaches (Longyang Gorge); 33.0-35.0 mW cm^{-2} sunlight intensity.

temperature to over 41 °C (Fig. 3h), surpassing the optimal growth temperature for *E. coli* at 37 °C.

In addition, we found that the bactericidal efficiency of 1 cm^2 Ag$_{SA+NP}$/ZIF was enhanced by ~4.0 log$_{10}$ after incubating *E. coli* to the logarithmic phase with saline (Fig. 4c), specifically referring to *E. coli* cultured under laboratory conditions without any stress resistance. The saline solution was prepared using the same river water, thus the different bactericidal activity toward stress-resistant bacteria and laboratory-cultured bacteria was not caused by other factors in the river water. This result confirms the stress resistance of *E. coli* at late stationary phase and highlights the necessity and precision of employing resistant bacteria to study the bactericidal activity of catalysts in actual aqueous environments. After 30 min of light exposure, 4 cm^2 Ag$_{SA+NP}$/ZIF dissolved Ag$^+$ and Zn^{2+} in 0.1 L river water, which were detected by an inductively coupled plasma mass spectrometry (ICP-MS) as 39.8 μg L^{-1} and 207.2 μg L^{-1}, respectively. These released metal ions demonstrated limited inhibitory efficiency against *E. coli* (Fig. 4d).

The time profiles of *E. coli* inactivation revealed that 4 cm^2 Ag$_{SA+NP}$/ZIF exhibited superior bactericidal efficiency compared to Ag$_{SA}$/ZIF and Ag$_{NP}$/ZIF (Fig. 4e). The converted atomic inactivation efficiency of Ag$_{SA+NP}$/ZIF within 30 min was 5.69 log$_{10}$ per mg Ag (Supplementary Table 4), which was over 195 and 2630 times higher than those of Ag$_{SA}$/ZIF (3.40 log$_{10}$ per mg Ag) and Ag$_{NP}$/ZIF (2.27 log$_{10}$ per mg Ag), respectively. The bactericidal efficiency of Ag$_{SA+NP}$/ZIF correlates with the temperature rise curve (Supplementary Fig. 9). During the initial 15 min, as the water temperature gradually rises, the bactericidal efficiency increases slowly. When the temperature reaches 41.8 °C after 15 min, there is a marked increase in bactericidal efficiency. This result suggests that the photothermal effect of Ag nanoparticles significantly enhances the bactericidal activity. In addition, the disinfection efficiencies of 4 cm^2 Ag$_{SA+NP}$/ZIF against Gram-positive bacteria *Staphylococcus aureus* (*S. aureus*) and virus MS2 were 2.10 log$_{10}$ and 5.77 log$_{10}$ (Fig. 4f), respectively, thereby confirming the high efficiency of Ag$_{SA+NP}$/ZIF to disinfect a broader range of microorganisms.

To verify the high bactericidal activity of the catalyst under varying water quality conditions, we studied its effectiveness against stress-resistant *E. coli* cultured in water from the middle reaches of

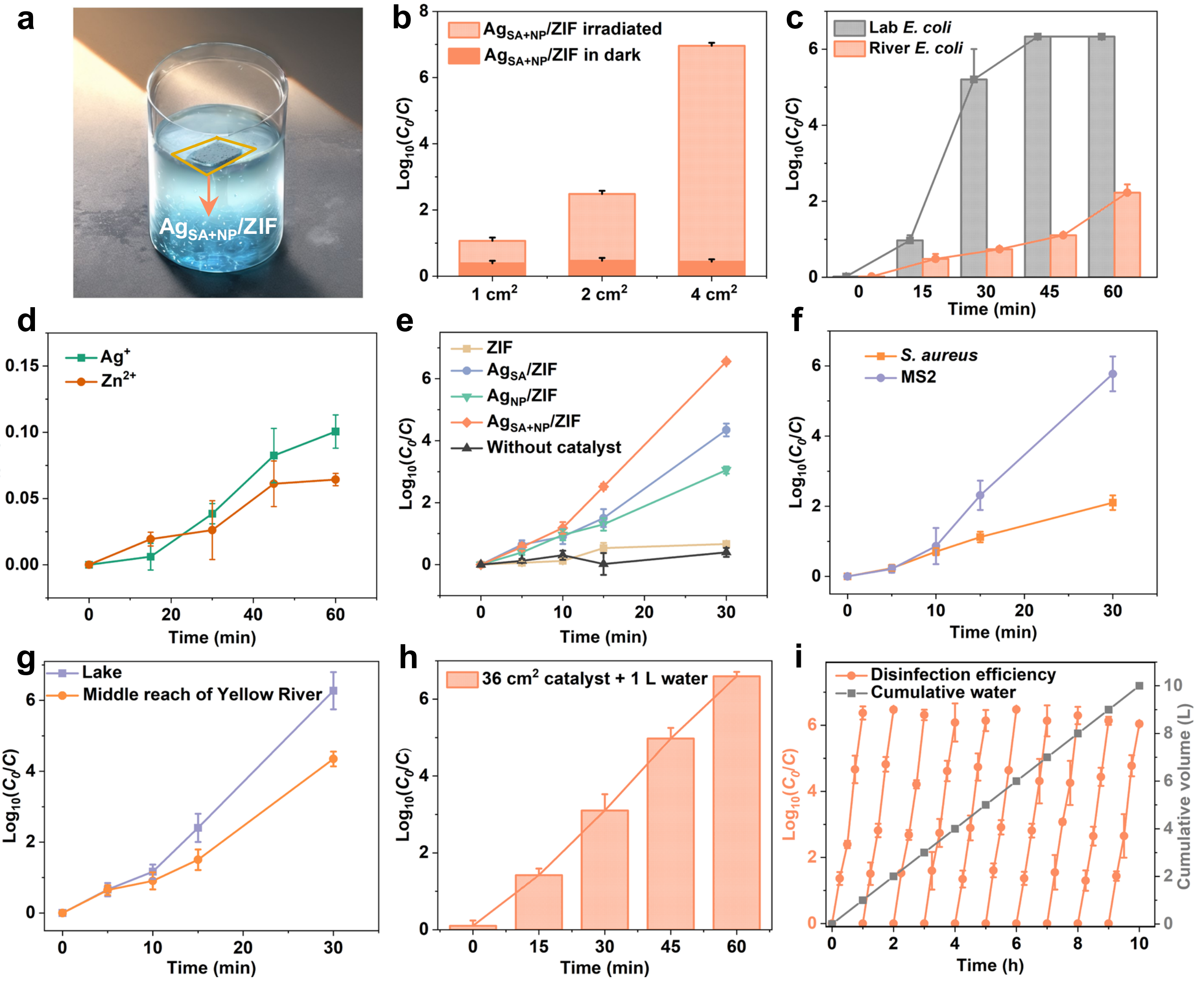

Fig. 4 | Photocatalytic disinfection performance under solar irradiation. **a** Disinfection operation schematic of Ag$_{SA+NP}$/ZIF. **b** Bactericidal efficiencies of 1, 2 and 4 cm^2 Ag$_{SA+NP}$/ZIF after 30 min solar irradiation in 0.1 L Yellow River water from upper reaches (Longyang Gorge). **c** Photocatalytic bactericidal performance of 1 cm^2 Ag$_{SA+NP}$/ZIF against *E. coli* in 0.1 L Yellow River water from upper reaches (Longyang Gorge) and laboratory-derived *E. coli* under solar irradiation. The lines represent time curves. **d** Time profiles of *E. coli* inactivation by 39.8 μg L^{-1} Ag$^+$ and 207.2 μg L^{-1} Zn^{2+}. **e** Time profiles of *E. coli* inactivation in 0.1 L Yellow River water from upper reaches (Longyang Gorge) by 4 cm^2 Ag$_{SA+NP}$/ZIF, Ag$_{SA}$/ZIF, Ag$_{NP}$/ZIF and ZIF-8-NH$_2$ photocatalysts. **f** Time profiles of *S. aureus* and virus MS2 inactivation in 0.1 L Yellow River water from upper reaches (Longyang Gorge) by 4 cm^2 Ag$_{SA+NP}$/ZIF photocatalyst. **g** Time profiles of *E. coli* inactivation in 0.1 L Yellow River water from middle reaches (Toudaoguai Station) and lake water (Shichahai) by 4 cm^2 Ag$_{SA+NP}$/ZIF photocatalysts. **h** *E. coli* inactivation efficiency in 1.0 L Yellow River water from upper reaches (Longyang Gorge) by four 3×3 cm^2 Ag$_{SA+NP}$/ZIF, corresponding to a total area of 36 cm^2. The line represents the time curve. **i** Disinfection efficiency of Ag$_{SA+NP}$/ZIF during recycling process. Experiments in **b**-**i** were conducted in triplicate, and the error bars represent the arithmetic mean ± standard deviation.

Yellow River (Toudaoguai Station) and lake water (Shichahai). Despite differences in water types (Supplementary Table 3), the 4 cm^2 Ag$_{SA+NP}$/ZIF achieved significant bacterial reductions of 4.35 log$_{10}$ in the middle reaches of Yellow River and 6.27 log$_{10}$ in lake water. The bactericidal activity in the middle reaches of the Yellow River was ~2 log$_{10}$ lower than that observed in the upper reaches (TOC: 5.49 mg L^{-1}), potentially attributed to higher concentrations of natural organic matter (TOC: 8.31 mg L^{-1}) in the middle reaches that effectively quench ROS. Additionally, the 4 cm^2 Ag$_{SA+NP}$/ZIF catalyst inactivated nearly 100% of the microorganisms in untreated real river water (Supplementary Fig. 10), demonstrating its potential for practical disinfection applications.

The application of Ag$_{SA+NP}$/ZIF was further extended to a large-scale water disinfection system in 1.0 L river water. As illustrated in Supplementary Fig. 11, four 3 × 3 cm^2 Ag$_{SA+NP}$/ZIF were employed to sterilize water with shaking. To consistently raise the water temperature above 41 °C, the system required a minimum catalyst area of 36 cm^2 and a velocity gradient of 70.7 s^{-1} (Supplementary Fig. 12a). This velocity corresponds to an extremely low rotational speed of ~100 rpm, which is insufficient to cause catalyst turnover and thereby fully expose the upper catalyst layer to light irradiation. The water temperature rose to 41.5 °C (Supplementary Fig. 12b) and 6.60 log$_{10}$ *E. coli* inactivation was achieved within 1.0 h (Fig. 4h) under solar irradiation of 33.0-35.0 mW cm^{-2}.

Durability experiments showed that the bactericidal activity of Ag$_{SA+NP}$/ZIF barely decreased after disinfecting a cumulative volume of 10.0 L water (Fig. 4i). This demonstrates its potential to meet the WHO recommended daily drinking water allocation of 8.0 L per person. The total loss of Ag compared to the total Ag present in the entire photocatalyst is 5.57% detected by ICP-MS. AC-HAADF-STEM image shows that Ag single atoms remain atomically dispersed and Ag nanoparticles are not depleted after the durability experiments (Supplementary Fig. 13), confirming the stability of Ag$_{SA+NP}$/ZIF. In addition, the average concentration of Ag$^+$ and Zn^{2+} dissolved by Ag$_{SA+NP}$/ZIF for a 1-h cycle was 40.2 μg L^{-1} and 331.4 μg L^{-1} (Supplementary Table 5), respectively. The Chinese standard for drinking water quality (GB 5749-2022) stipulates that the concentration of Ag and Zn in drinking water should not exceed 50.0 $\mu g\ L^{-1}$ and 1000.0 $\mu g\ L^{-1}$, respectively, which indicated that our detected levels are complying.

The price of Ag_{SA+NP}/ZIF-based water disinfection was also evaluated as shown in Supplementary Table 6. Four 3 × 3 cm^2 Ag_{SA+NP}/ZIF can disinfect at least 10.0 L water at a cost of $0.27, which is relatively higher compared to conventional treatment technologies such as chlorine dioxide disinfection, which costs $0.11. This higher cost arises from the synthesis process, which is conducted on a laboratory scale utilizing small packages of high-purity reagents (analytical reagent grade). However, the cost could be substantially reduced by scaling production to an industrial level, utilizing more cost-effective, technical-grade reagents. This adjustment could satisfy the economic and practical demands for disinfection applications.

Photothermal effect synergizes water disinfection

Previous studies have demonstrated that the photothermal action of plasmonic nanoparticle promotes protein aggregation in tumor cells and interferes their DNA damage repair capabilities[22]. However, the impacts of photothermal action on bacterial cells remain unclear. We hypothesize that the bacterial stress-resistant systems may potentially be compromised primarily due to the photothermal heating of Ag nanoparticles, resulting in increased bacterial susceptibility to ROS.

The transcriptomic analysis was employed to elucidate the impact of photothermal effect on the stress-resistant system of *E. coli* at the gene expression level. Compared to Ag_{SA}/ZIF treated *E. coli*, a total of 287 genes exhibited differential expression in *E. coli* treated with Ag_{SA+NP}/ZIF for 15 min ($|\log_2$ fold-change$| \geq 1$, $p < 0.05$), with 121 genes being downregulated and 166 genes being up-regulated (Fig. 5a). Gene Ontology (GO) functional enrichment analysis results shown in Fig. 5b and Supplementary Table 7 indicate that the downregulated genes are enriched in response to hydrogen peroxide, response to reactive oxygen species, and DNA repair items (p-value < 0.05), with the rich factors of 0.16, 0.11 and 0.07, respectively. The expression of downregulated genes in Ag_{SA}/ZIF-treated *E. coli* was 2286 (Supplementary Fig. 14). However, no significant enrichment was found in the aforementioned three GO categories (Supplementary Table 8), which suggests that the photothermal effect of Ag_{SA+NP}/ZIF at 41.8 °C can decrease the bacterial resistance to ROS and DNA repair ability[45], with a higher proportion of downregulated genes responding to ROS (particularly hydrogen peroxide) compared to those involved in DNA damage repair. This result was further validated through disinfection experiments (Supplementary Fig. 15), wherein the 30-min inactivation of *E. coli* exhibited a >2.0 log increase when the temperature of the Ag_{SA}/ZIF system was elevated from 36 °C to 41 °C, approximating the temperature of the Ag_{SA+NP}/ZIF system. It is worth noting that the sole increase in temperature to 41 °C did not result in a significant impact on bacterial survival.

Given that the bacterial anti-stress system involves the removal of intracellular ROS, the fluorescent probe 2,7-dichlorodihydrofluorescein diacetate (DCFH-DA) was employed in conjunction with

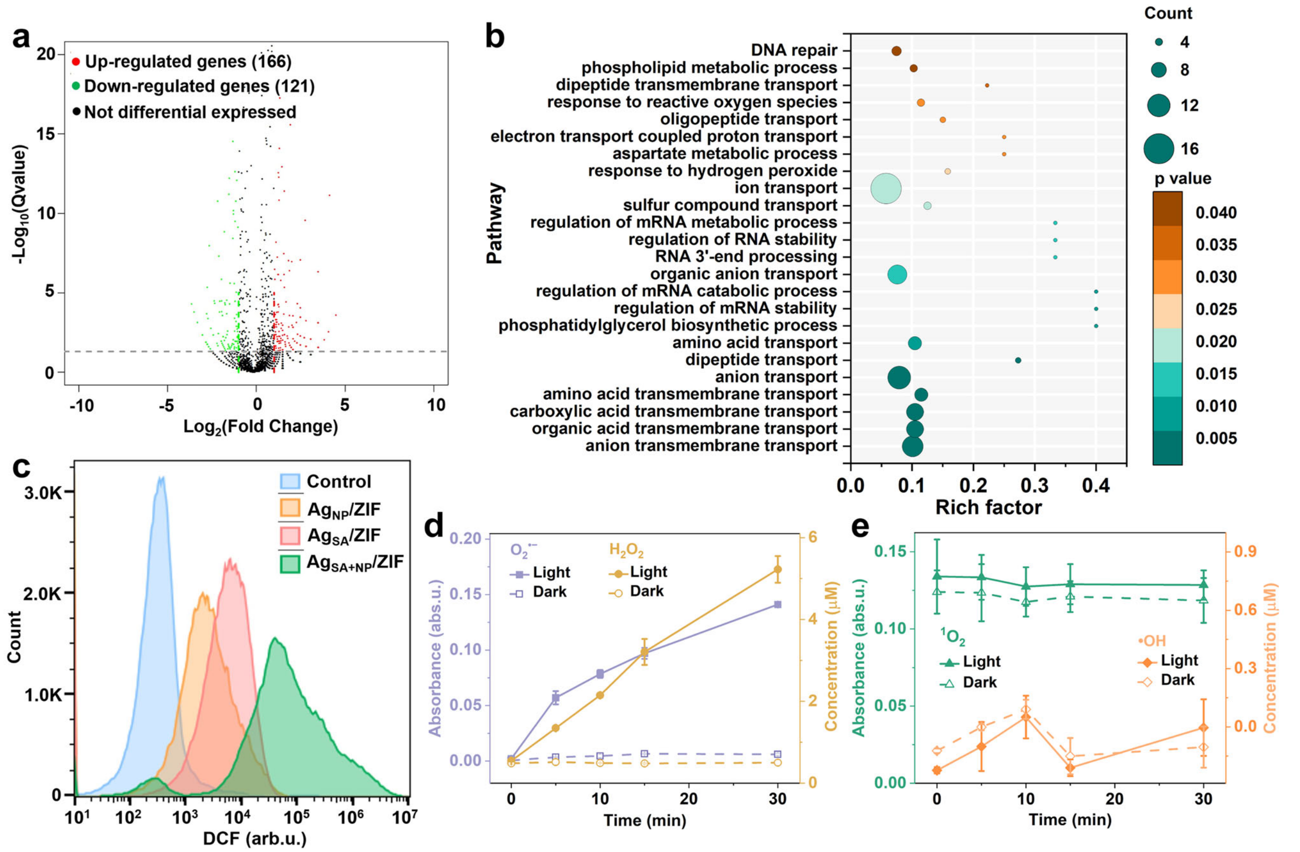

Fig. 5 | Synergistic disinfection mechanism elucidation. **a** Volcano plot of RNA sequencing data from *E. coli* culture exposed to Ag_{SA+NP}/ZIF for 15 min. **b** GO functional enrichment of the downregulated genes subset in *E. coli* exposure to Ag_{SA+NP}/ZIF for 15 min. Rich factor refers to the ratio of the number of differentially expressed genes to the total number of all annotated genes located in the same term. The dot color represents the p-value, and the dot size represents the number of differentially expressed genes in each term. **c** Intracellular ROS levels of *E. coli* exposed to monolithic photocatalysts for 15 min. **d** $O_2^{\bullet-}$ generation kinetics indicated by the absorbance of formazan dye that generated by the reaction of NBT with $O_2^{\bullet-}$ and H_2O_2 generation kinetics of Ag_{SA+NP}/ZIF. **e** •OH generation kinetics of Ag_{SA+NP}/ZIF and time profile of ABMDMA degradation by Ag_{SA+NP}/ZIF-generated $^1O_2$. Reaction conditions: 4 cm^2 monolithic photocatalysts; 0.1 L Yellow River water from upper reaches (Longyang Gorge); 33.0-35.0 mW cm^{-2} sunlight intensity. Experiments in **d** and **e** were conducted in triplicate, and the error bars represent the arithmetic mean ± standard deviation.

flow cytometry for semi-quantitative analysis of the total intracellular ROS accumulation. In the early phase of the reaction, the mean fluorescence intensity across the groups exhibited no significant variation, suggesting a similar accumulation of ROS (Supplementary Fig. 16). After 15 min (Fig. 5c), the mean fluorescence intensity in the Ag_{SA+NP}/ZIF-treated cells increased 33.6-fold when compared to that in the Ag_{SA}/ZIF-treated cells. Upon comparing the mean fluorescence intensity between groups following 30 min of reaction (Supplementary Fig. 16), the observed trend remained consistent. This phenomenon can be attributed to the photothermal effect of Ag_{SA+NP}/ZIF, which effectively down-regulates the cellular response to ROS and consequently hinders their removal[45].

The mean fluorescence intensity of Ag_{SA}/ZIF-treated cells was 1.7 times higher compared to that of Ag_{NP}/ZIF-treated cells (Fig. 5c). This suggests that a sole photothermal effect from Ag nanoparticles is not significant to elevate intracellular ROS levels in *E. coli*. The reaction system was subsequently treated with 20 μM melatonin to eliminate exogenous ROS, while low levels of endogenous ROS were detected in *E. coli* as indicated by low 2,7-dichlorofluorescein (DCF) intensity (Supplementary Fig. 17). Therefore, the accumulated intracellular ROS mainly originated from exogenous ROS generated by the photocatalyst. The absence of Ag single-atom sites in Ag_{NP}/ZIF leads to insufficient generation of exogenous ROS, whose transmembrane import is the main cause of the rise in intracellular ROS levels. Thus, Ag_{SA+NP}/ZIF, which possesses atomically dispersed Ag sites and plasmonic Ag nanoparticles, could respectively facilitate intracellular ROS generation and accumulation in cells, thereby synergistically inactivating stress-resistant *E. coli* cells.

To comprehend the disinfection mechanisms associated with extracellular ROS, nitro blue tetrazolium chloride (NBT, $O_2^{\bullet-}$-specific indicator), coumarin (Cou, •OH-specific indicator), 9,10-anthracenediyl-bis(methylene)dimalonic acid (ABMDMA, $^1O_2$-specific indicator), *p*-hydroxyphenylacetic acid (HPA, H_2O_2-specific indicator) were applied to monitor specific ROS generated by Ag_{SA+NP}/ZIF in deionize water. Under solar irradiation, the absorbance of formazan dye generated by the reaction of NBT with $O_2^{\bullet-}$ increases in a time-dependent manner (Fig. 5d). Similarly, the fluorescent products generated by the reaction of H_2O_2 with HPA were detected, and the concentration of H_2O_2 after 30 min reaction was 5.22 μmol L^{-1} (Fig. 5d). In the disinfection system, H_2O_2 can be generated through both the oxygen reduction pathway ($O_2 + 2H^+ + 2e^- \rightarrow H_2O_2$) and the disproportionation reaction of $O_2^{\bullet-}$ ($2O_2^{\bullet-} + H^+ + H_2O \rightarrow H_2O_2 + O_2 + OH^-$)[43]. When investigating the production of •OH and $^1O_2$, we found no significant increase in fluorescence intensity of Cou and decrease in absorbance of ABMDM (Fig. 5e), indicating the absence of detectable levels of •OH and $^1O_2$. •OH generation is thermodynamically unfavorable as the valence band potential of Ag_{SA+NP}/ZIF (2.35 V vs. NHE) may not be sufficient to oxidize water (2.68 V vs. NHE)[43].

The generation of extracellular ROS was further validated using two independent tests: electron paramagnetic resonance (EPR) spectroscopy and scavenger quenching analysis. A characteristic 5-tert-butoxycarbonyl-5-methyl-1-pyrroline N-oxide (BMPO)-$O_2^{\bullet-}$ peak indicated the production of $O_2^{\bullet-}$ (Supplementary Fig. 18a), while no EPR signals were detected for •OH and $^1O_2$ (Supplementary Fig. 18b, c). Scavenging H_2O_2 and $O_2^{\bullet-}$ significantly reduced *E. coli* inactivation efficiency (Supplementary Fig. 19). Therefore, $O_2^{\bullet-}$ and H_2O_2 are the primary ROS responsible for Ag_{SA+NP}/ZIF disinfection, with h^+ playing a secondary role in *E. coli* inactivation. It is worth mentioning that $O_2^{\bullet-}$ and H_2O_2 both exhibit longer lifespans compared to •OH and elicit longer disinfection power[46,47]. The direct contact between bacterial cells and photocatalyst is less important for our disinfection system, as H_2O_2 and $O_2^{\bullet-}$ can effectively diffuse into the bulk solution and inactivate bacterial cells that are not in contact with the photocatalyst[48].

TEM analysis showed no significant damage to the cell membrane structure of Ag_{SA+NP}/ZIF-treated bacteria compared to untreated bacteria (Supplementary Fig. 20a, b). Bacteria with intact membrane selectivity remain impermeable to propidium iodide (PI) staining but can be stained by SYTO9, while the bacteria with disrupted membrane selectivity are PI-permeable. Approximately 71.2% of bacteria exhibited disrupted membrane selectivity after 30-min treatment with Ag_{SA+NP}/ZIF (Supplementary Fig. 20c-e). The disruption interfered with normal cellular transport, as evidenced by the down-regulation of genes related to electron transport coupled proton transport, amino acid transmembrane transport, and anion transmembrane transport (Fig. 5b). Quantitative polymerase chain reaction (qPCR) analysis revealed a 1.27 log reduction in the 16s gene copy number in the Ag_{SA+NP}/ZIF-treated group after 30 min (Supplementary Fig. 21), indicating significant DNA damage. This result is consistent with transcriptome analysis (Fig. 5b) showing down-regulation of DNA repair genes. While direct structural damage to the cell membrane was minimal due to limited contact, Ag_{SA+NP}/ZIF effectively compromised membrane selectivity and induced intracellular DNA degradation through ROS generation.

Discussion

In this study, we successfully developed a floatable monolithic Ag_{SA+NP}/ZIF photocatalyst for water disinfection. Atomically dispersed Ag promotes charge transfer to facilitate the generation of H_2O_2 and $O_2^{\bullet-}$. Transcriptomics analysis suggests that the photothermal effect of plasmonic Ag nanoparticles disrupted the anti-stress system of *E. coli*, thereby reducing their resistance to ROS. Under solar irradiation, the synergistic effect of Ag single atoms and nanoparticles enables 36 cm^2 Ag_{SA+NP}/ZIF to disinfect at least 10.0 L of surface water, which meets the WHO's recommended daily per capita drinking water allocation. The present study demonstrates a potential approach to addressing the challenges of low photocatalytic disinfection efficiency in real-world water and the limited recyclability of traditional granular photocatalysts. It provides a foundation for sustainable and environmentally friendly POU water disinfection. However, the findings are based on the evaluation of a single photocatalyst under controlled laboratory conditions. To apply this approach in real-world settings, particularly in off-grid regions, requires overcoming several critical challenges. These include reducing material costs, improving scalability, and ensuring sustained photocatalytic performance under varying environmental conditions. Furthermore, overcoming practical obstacles such as efficient system integration and optimizing energy consumption is essential for the successful deployment and long-term viability of this technology in large-scale water treatment systems.

Methods

Monolithic ZIF-8-NH_2 support preparation

Commercially available sponges are mainly composed of melamine and have a porous structure with a density of 45.0 mg cm^{-3}. The 4×2×1 cm^3 three-dimensional melamine sponge was utilized as a substrate to absorb 10 mL 2.0 wt% aqueous sodium alginate solution (99%; Aladdin), followed by immersion in 30 mL 2.0 wt% zinc nitrate hexahydrate solution (99%; Aladdin) for 12 h to form gel-coated sponge. The gel-coated sponge was then placed in an oven and dried at 150 °C for 2 h to facilitate water evaporation and obtain a desiccated sponge. Then 0.279 g 2-methylimidazole (99%; Sigma Aldrich) and 0.08 g 2-aminobenzimidazole (97%; Aladdin) were placed at the bottom of the customized Teflon-lined stainless-steel autoclave, and a 1×1×0.2 cm^3 dried sponge situated above the organic ligands[49]. The dried sponge and organic ligand powder were kept separate. The autoclave was heated at 150 °C for ligand evaporation and deposition. After the reaction for 2 h, the obtained monolithic ZIF-8-NH_2 support was washed three times with deionized water and dried in a vacuum oven at 60 °C for 12 h. Larger size monolithic ZIF-8-NH_2 was prepared through proportionally increasing the amount of reaction reagents.

Monolithic photocatalyst preparation

The $1 \times 1 \times 0.2\,\mathrm{cm}^3$ monolithic ZIF-8-NH_2 sponge and 120 μL 67.9 mg mL^{-1} silver nitrate solution (99.9%; Sigma Aldrich) were added to 10 mL of deionized water and left for 12 h to sufficiently adsorb Ag ions. The mixture was then snap-frozen in liquid nitrogen and the upper surface ($1\times1\,\mathrm{cm}^2$) of monolithic ZIF-8-NH_2 sponge was irradiated under UV lamp (Beijing Perfectlight, PCX-50C Discover) with a peak intensity at 365 nm for 10 min. The light intensity on the reaction solution surface was 52.8 mW cm^{-2} as measured using the UV power meter (UV-A, Beijing Normal University Photoelectric Instrument Factory). The ambient temperature is maintained at 25 °C to allow the ice to melt during irradiation. The ice lattice inhibited nucleation[50], thus reducing Ag ions to single atoms. With the melting of ice, a portion of Ag was transformed into nanoparticles, leading to the formation of photocatalysts that incorporate both Ag single atoms and Ag nanoparticles. The obtained monolithic $\mathrm{Ag_{SA+NP}}$/ZIF was washed three times with deionized water and dried in a vacuum oven at 60 °C. In addition, the synthesis of $\mathrm{Ag_{SA}}$/ZIF was carried out under the same conditions except that the ambient temperature was kept at 0 °C. $\mathrm{Ag_{NP}}$/ZIF was synthesized by the same process without liquid nitrogen freezing.

Material characterization

The microstructure and morphology of photocatalysts were obtained by SEM (FEI Inspect F50) and high-resolution TEM (FEI Talos F200S). Ag single-atom was observed by AC-HAADF-STEM (Titan Themis 60-300) operated at 200 kV, coupled with a probe spherical aberration corrector. Atomic dispersion and coordination environment of Ag species were confirmed by XAFS measurements, which were carried out on the sample at 11S2 X-ray absorption beamline of Aichi Synchrotron Radiation Center. The radiation was monochromatized by a Si (111) double-crystal monochromator. The measurements were carried out with a passivated implanted planar silicon fluorescence detector using Ag foil to calibrate the energy. XAFS data was analyzed by the Athena (version 0.9.26) and Artemis software (version 0.9.26) as shown in Supplementary Table 1 and Supplementary Note. The Ag loading content and dissolved Ag^+ concentration of photocatalysts were measured by ICP-OES (Agilent 725-ES) and ICP-MS (Agilent 7700), respectively. The UV-Vis diffuse reflectance spectra of the photocatalysts were recorded on a PE Lambda750 spectrophotometer. The steady-state and time-resolved photoluminescence spectra were carried out for the characterization of electron-hole pairs separation using the Hitachi F-7000 spectrophotometer and Edinburgh FLS1000 spectrofluorometer with an excitation wavelength of 375 nm, respectively. The average lifetime was obtained by fitting the luminescence decay curves with a biexponential function. Electrochemical impedance spectroscopy and Mott–Schottky measurements were performed in 0.5 M Na_2SO_4 (99%; Aladdin) solution by using a CHI-660E electrochemical workstation (Shanghai, China). Photothermal properties of photocatalysts were characterized by a digital infrared thermal camera (FLIR E50).

Since Ag single atoms and Ag nanoparticles account for 100% of the silver content, the proportion of Ag nanoparticles can be deduced from the Ag single atoms proportion. The proportion of Ag single atoms can be estimated using the average Ag–N coordination number[51]. The Ag–N coordination number of atomically dispersed Ag sites in $\mathrm{Ag_{SA}}$/ZIF catalyst is 3.2. Therefore, the average Ag–N coordination number in $\mathrm{Ag_{SA+NP}}$/ZIF catalyst can be calculated by the following equation:

$$n = \frac{N_{Ag-N}}{N_{Ag}} = \frac{N_{Ag} * X_1 * 3.2}{N_{Ag}} = X_1 * 3.2 \tag{1}$$

where n represents the coordination number of Ag–N in $\mathrm{Ag_{SA+NP}}$/ZIF catalyst, N_{Ag-N} represents the number of total Ag–N bond, N_{Ag} represents the number of total Ag atoms, and X_1 represents the proportion of Ag single atoms in $\mathrm{Ag_{SA+NP}}$/ZIF catalyst. Therefore, Using the observed coordination number (Supplementary Table 1), the proportion of Ag single atoms in the $\mathrm{Ag_{SA+NP}}$/ZIF catalyst can be approximately calculated as follow:

$$X_1 = n/3.2 \tag{2}$$

Evaluation of the photocatalytic disinfection performance

River water and lake water with various water qualities, including the upper reaches of Yellow River (Longyang Gorge, Qinghai Province, China), the middle reaches of Yellow River (Toudaoguai Station, Inner Mongolia, China), and lake water (Shichahai, Beijing, China), were collected to test disinfection activity. The chemical parameters of the water samples were detected by the water quality analyzer (ProQuatro, YSI) as shown in Supplementary Table 3. Briefly, river water was filtered through cellulose membranes with the pore size of 0.45 μm to remove suspended sediment. The filtered river water was supplemented with 100 mg L^{-1} of yeast extract and autoclaved to remove background microorganisms. This sterilized water samples were used to grow bacteria for disinfection experiments and RNA extraction.

E. coli BW25113 purchased from the Coli Genetic Stock Center (CGSC, Yale University, USA) was used as the model microorganism. 5 μL of *E. coli* strain were inoculated in 5 mL of Luria-Bertani (LB) medium at 37 °C for 12 h, then 5 mL of culture was transferred to 50 mL of LB medium and cultured for another 2 h. *E. coli* culture was collected and washed by centrifugation, and re-suspended in 50 mL sterilized river water to achieve an optical density of 0.06 at 670 nm ($\approx 1\times10^8$ bacteria mL^{-1}). *E. coli* cells was allowed to stand in the sterilized river water at 25 °C for 24 h to acclimatize to the new growth conditions and collected by centrifugation. Collected *E. coli* cells were then transferred to 50 mL fresh sterilized river water for 48 h incubation with shaking at 160 rpm at 25 °C to reach the late stationary phase (Supplementary Fig. 22). This growth phase better resembles bacterial cell conditions observed in oligotrophic surface water, where cellular responses are typically activated to counter starvation and other environmental stressors[17]. After 48 h of incubation, *E. coli* cultures were diluted 100-fold by fresh river water for disinfection testing. The monolithic photocatalyst with surface area of 1-4 cm^2 was plunged into 0.1 L *E. coli* suspension and irradiated without any agitation under sunlight (14:00-15:00 pm in September in Beijing, China) with a light intensity of 33.0-35.0 mW cm^{-2}. For large-scale water disinfection, 1.0 L *E. coli* suspension was placed in a 2.0 L beaker and shaken on a shaker at a constant velocity. The Camp-Stein velocity gradient (*G*) for a shaker was calculated by the following Eq. (3):

$$G = \sqrt{\frac{P}{p\upsilon}} \tag{3}$$

where P represents the power input into the control volume (0-14 W), p represents the density of the fluid (997 kg m^{-3}), υ represents the volume of the fluid (0.001 m^3), and ∀ represents volume of the control volume (0.002 m^3).

Five mL of the sample was carefully pipetted out at the sampling time and diluted 10, 100, and 1000 times with sterile normal saline, respectively. 100 μL of the diluted *E. coli* samples were spread evenly on LB agar plates and incubated at 37 °C overnight for colony counting. The concentration of *E. coli* was calculated by the formula: $C = n \times$ dilution times $\times\, 10$, where C represented the concentration of *E. coli* in the sample (CFU mL^{-1}) and n represented the number of colonies. The concentration of *E. coli* without photocatalytic treatment was represented by C_0, thus the bactericidal efficiency was expressed as

$\text{Log}_{10}(C_0/C)$. Each experiment was performed three times independently.

Transcriptome analysis

To analyze the impact of photothermal stress on biological functions in *E. coli*, transcriptomics analysis was conducted by extracting RNA from *E. coli* cells exposed to Ag_{SA}/ZIF and $\text{Ag}_{\text{SA+NP}}$/ZIF for 15 min, as well as a control group. Total RNA extraction was performed using the Total RNA Extractor kit (Sangon Biotech, Shanghai) for subsequent RNA-seq analysis. The quality and quantity of total isolated RNA in the samples were analyzed by a Qubit 2.0 fluorometer using Qubit RNA Quantification Kit (Invitrogen). The rRNA depletion was carried out using Ribo-off rRNA Depletion Kit (Vazyme, Nanjing) according to manufacturer's specifications. The rRNA-deleted samples were further purified to obtain purified mRNA, and the RNA libraries of purified mRNA were constructed with VAHTS Stranded mRNA-seq V3 Library Prep Kit for Illumina (Vazyme, Nanjing). The quality of the RNA libraries was checked by 8% polyacrylamide gel electrophoresis. After that, all libraries were sequenced using an Illumina HiSeq 3000 system with paired-end 150 base-pair reads. Significantly differentially expressed genes were analyzed by DESeq2 R-package (version 1. 12. 4) with a screening condition of $p\text{-value} \le 0.05$ and $|\log_2 \text{fold-change}| \ge 1$. GO enrichment analysis was performed by topGO R-package (version 2. 24. 0) to evaluate the biological function enrichment corresponding to the differentially expressed genes sets. In general, GO terms with an adjusted $p\text{-value} < 0.05$ were considered significantly enriched.

ROS measurements

When bacterial cells are exposure to monolithic photocatalyst, ROS may penetrate the cell membrane causing intracellular ROS accumulation, which was detected by using the fluorescent probe DCFH-DA (99.81%; MCE) in conjunction with flow cytometer (ACEA NoveCyte$^{\text{TM}}$). DCFH-DA can freely penetrate cellular membranes and undergo intracellular hydrolysis by esterase, resulting in the formation of 2,7-dichlorodihydrofluorescein (DCFH) that becomes sequestered within the cytomembrane. Subsequently, intracellular ROS oxidizes DCFH to generate fluorescent DCF, exhibiting maximum excitation and emission wavelengths at 488 nm and 525 nm, respectively. Briefly, *E. coli* treated for 0-30 min in the photocatalytic disinfection system were incubated with DCFH-DA at a concentration of 25 μM for 30 min at 37 °C. The bacterial cells after incubation were collected and washed with saline (85% NaCl solution) to remove excess fluorescent probe. The flow cytometer laser was selected to be 488 nm, and the number of the collected cells was 100,000. The sample collection speed was adjusted to the low mode (14 $\mu\text{L min}^{-1}$), and the threshold of FSC-H was set to 1000. The mean intracellular fluorescence intensity of bacteria was analyzed by FlowJo V10 software.

For H_2O_2 concentration detection, a working solution was prepared by adding 2.7 mg of *p*-hydroxyphenylacetic acid (98%; Aladdin) and 1 mg of horseradish peroxidase (200 U mg^{-1}; Aladdin) to 10 mL of potassium hydrogen phthalate buffer solution (8.2 g L^{-1}). Subsequently, 50 μL of working solution was added to 1 mL sample, diluted with 1 mL deionized water, and the reaction was quenched by adding 1 mL 0.1 M NaOH (99%; Aladdin) after 10 min. The fluorescence spectra of samples were measured with an excitation wavelength of 315 nm and detected at an emission wavelength of 409 nm. For the detection of $O_2^{\bullet-}$, 30 μL of 1 mM NBT (98%; Aladdin) dissolved in dimethyl sulfoxide (99.8%; Aladdin) and 3 mL of sample were mixed and incubated for 10 min. The reaction generated formazan dye with maximum absorbance at 680 nm was detected by UV-Vis spectrophotometer. The concentration of •OH generation was determined by the fluorescence method using coumarin as a probe[43]. One mM coumarin (99%; Aladdin) and $\text{Ag}_{\text{SA+NP}}$/ZIF were mixed in 0.1 L water. Coumarin reacts with •OH to produce 7-hydroxycoumarin, which can emit fluorescence at 451 nm with excitation wavelength of 332 nm. The presence of $^1O_2$ was detected by using ABMDMA (90%; MCE) as a sensitive indicator. The bleaching of ABMDMA by singlet oxygen resulted in a decrease in its absorbance at 400 nm. 0.5 mL ABMDMA (2 mM) and $\text{Ag}_{\text{SA+NP}}$/ZIF were mixed in 0.1 L water. The consumption of ABMDMA was monitored by recording the absorbance at 400 nm with a UV-Vis spectrophotometer. The sunlight intensity was 33.0-35.0 mW cm^{-2} and $\text{Ag}_{\text{SA+NP}}$/ZIF size is 4 cm^2.

ROS were detected by EPR spectroscopy on a Bruker A300 spectrometer operating at an X-band frequency of 9.85 GHz. The monolithic catalyst was crushed and prepared as a suspension sample (100 mg L^{-1}). Ten μL of 50 mg mL^{-1} BMPO (99%; Aladdin) and 10 μL of water were mixed with 30 μL of catalyst sample. The resulting liquid was aspirated using a capillary tube, followed by light exposure for 10 min to detect both •OH and $O_2^{\bullet-}$. For the detection of •OH alone, the procedure was modified by substituting 10 μL of water with 10 μL of superoxide dismutase (SOD, 5 U mL^{-1}; Aladdin) to quench $O_2^{\bullet-}$. To detect $^1O_2$, 25 μL of 10 mM 2,2,6,6-tetramethylpiperidine (TEMP, 99%; Aladdin) was mixed with 25 μL of catalyst sample, and measurements were conducted under both 10-min light exposure and in dark conditions.

The scavengers used for •OH elimination, H_2O_2 neutralization, $O_2^{\bullet-}$ scavenging, hole scavenger, electron capture, and $^1O_2$ quenching were 2.5 mM isopropanol (99.5%; Sigma), catalase (CAT, 300 U mL^{-1}; Sigma), SOD (400 U mL^{-1}; Sigma), 2.5 mM sodium oxalate (99.5%; Sigma), 2.5 mM sodium chromate (Cr(VI)), (99.5%; Sigma), and 2.5 mM furfuryl alcohol (99%; Sigma), respectively. The scavengers applied in this study showed no significant impact on bacterial activity (Supplementary Fig. 23). These scavengers were added to the bacterial suspension prior to illumination. Bacterial concentrations in solution were determined at different time intervals using standard spread plating method. Each sample was serially diluted and plated in triplicate onto nutrient agar before incubation at 37 °C for 24 h.

Membrane damage and DNA degradation

Cell membrane structure damage was analyzed by TEM on sliced bacterial specimen. Briefly, the harvested bacterial cells were first fixed in a solution of 4% paraformaldehyde (95%; Aladdin) and 2.5% glutaraldehyde (50%; Aladdin) for 12 h at 4 °C. The samples were then infiltrated and embedded in Spurr's resin with propylene oxide (99%; Aladdin) and cured overnight at 70 °C. Subsequently, ultrathin sections were prepared using an ultramicrotome (MT-X, RMC) and examined with a Hitachi H7700 TEM operated at 75 kV. The collected samples were stained with LIVE/DEAD BacLight Viability Kit (Thermo Fisher scientific) and analyzed with flow cytometry (ACEA NoveCyte$^{\text{TM}}$). This kit contains two fluorescent nucleic acids dyes, namely SYTO 9 and PI. *E. coli* cells with intact membrane can only be stained green by SYTO 9 (Ex. 488 nm and Em. 530 nm), and *E. coli* cells with disrupted membrane selectivity can be stained red by PI (Ex. 488 nm and Em. 630 nm). The defined gates include: complete membrane destruction (*Q1*), disrupted membrane selectivity (*Q2*), impurities (*Q3*), and intact membrane (*Q4*). The proportion of bacteria (*P*) with disrupted membrane selectivity was determined using Eq. (4):

$$\text{P} = \frac{\text{Q1} + \text{Q2}}{\text{Q1} + \text{Q2} + \text{Q4}} \tag{4}$$

The qPCR amplicon targeting the 16S gene was employed for highly sensitive detection of DNA damage[52], and the primer sequence can be found in Supplementary Table 9. The qPCR reaction parameters were as follows: pre-incubation at 95 °C for 3 min; amplification of 35 cycles with each cycle being 95 °C for 30 s, 60 °C for 30 s, and 72 °C for 45 s; melt curve generation at 90 °C for 10 s, and 60 °C for 60 s; and a gradual heating to 90 °C at a rate of 0.03 °C s^{-1}.

Electromagnetic simulation

To explain the enhancement local electromagnetic field near the surface between the Ag nanoparticles and the ZIF-8-NH_2, we used COMSOL Multiphysics (version 6.2), employing the Electromagnetic Waves, Frequency Domain physics interface and Wavelength Domain in the optics module. Briefly, the refractive indices of Ag nanoparticles and air were obtained from the COMSOL built-in material library, while the refractive index of ZIF-8-NH_2 substrate was set to 1.38. A series of parallel simulations is designed to show the effect of varying ZIF-8-NH_2 thickness and Ag nanoparticle size on the electromagnetic field at the interface between Ag nanoparticle and ZIF-8-NH_2 under 450 nm irradiation. The variations include ZIF-8-NH_2 thicknesses ranging from 1 to 15 nm and Ag nanoparticle radius of 1, 3.5, 5, 6.5, 8 nm. The geometric model consisted of one Ag spherical particle on the center of a ZIF-8-NH_2 substrate as shown in the Supplementary Fig. 24. Incident light with a wavelength of 450 nm was directed vertically downward pointing the x-y plane. The air domain is confined by the inclusion of a Perfect Matching Layer (PML), which restricts the model to a specific area of interest to conserve computing resources while maintaining accuracy consistent with results from a large, unrestricted solution domain[53]. The solution within this domain remains unaffected by the introduced PML. The Perfect Electrical Conductor (PEC) boundary conditions were used on the x-y symmetry plane. A Frequency Domain was defined as the initial incident electric field E_O, serving as the background for the scattered field. The distribution of $|E|/|E_O|$ was computed to analyze the electromagnetic field enhancement at the interface of Ag nanoparticles loaded on ZIF-8-NH_2. The COMSOL simulation parameters are provided in Supplementary Method and Supplementary Table 10.

Reporting summary

Further information on research design is available in the Nature Portfolio Reporting Summary linked to this article.

Data availability

The RNA sequencing data generated in this study have been deposited in the NCBI Sequence Read Archive (SRA) database under accession code PRJNA1199748. Data supporting the findings of this work are available within the paper and its Supplementary Information files. Source data are provided with this paper. The full image data are available from the corresponding author upon request. Source data are provided with this paper.

References

1. World Health Organization & United Nations Children's Fund (UNICEF). *Progress on Sanitation and Drinking Water—2015 Update and MDG Assessment* (World Health Organization, Geneva, 2015).
2. Alvarez, P. J. J., Chan, C. K., Elimelech, M., Halas, N. J. & Villagrán, D. Emerging opportunities for nanotechnology to enhance water security. *Nat. Nanotechnol.* **13**, 634–641 (2018).
3. Liu, L. et al. Global, regional, and national causes of child mortality: an updated systematic analysis for 2010 with time trends since 2000. *The Lancet* **379**, 2151–2161 (2012).
4. Prüss-Ustün, A. et al. Burden of disease from inadequate water, sanitation and hygiene in low- and middle-income settings: a retrospective analysis of data from 145 countries. *Trop. Med. Int. Health* **19**, 894–905 (2014).
5. Chu, C., Ryberg, E. C., Loeb, S. K., Suh, M.-J. & Kim, J.-H. Water Disinfection in Rural Areas Demands Unconventional Solar Technologies. *Acc. Chem. Res.* **52**, 1187–1195 (2019).
6. Richards, T. et al. A residue-free approach to water disinfection using catalytic in situ generation of reactive oxygen species. *Nat. Catal.* **4**, 575–585 (2021).
7. Montgomery, M. A. & Elimelech, M. Water And Sanitation in Developing Countries: Including Health in the Equation. *Environ. Sci. Technol.* **41**, 17–24 (2007).
8. Smieja, J. A. Household Water Treatments in Developing Countries. *J. Chem. Educ.* **88**, 549–553 (2011).
9. Palika, A. et al. An antiviral trap made of protein nanofibrils and iron oxyhydroxide nanoparticles. *Nat. Nanotechnol.* **16**, 918–925 (2021).
10. Zhou, X. et al. Bacteria inactivation by sulfate radical: progress and non-negligible disinfection by-products. *Front. Environ. Sci. Eng.* **17**, 29 (2023).
11. Chen, R., Chen, S., Wang, L. & Wang, D. Nanoscale Metal Particle Modified Single-Atom Catalyst: Synthesis, Characterization, and Application. *Adv. Mater.* **36**, 2304713 (2024).
12. Gloag, L., Somerville, S. V., Gooding, J. J. & Tilley, R. D. Co-catalytic metal–support interactions in single-atom electrocatalysts. *Nat. Rev. Mater.* **9**, 173–189 (2024).
13. Liu, Y., Zhao, H. & Zhao, Y. Designing Efficient Single Metal Atom Biocatalysts at the Atomic Structure Level. *Angew. Chem. Int. Ed.* **63**, e202315933 (2024).
14. Li, Y. et al. Visible-light-driven photocatalytic disinfection mechanism of Pb-$BiFeO_3$/rGO photocatalyst. *Water Res.* **161**, 251–261 (2019).
15. Zhou, Z. et al. Structural insights into the inhibition of bacterial RecA by naphthalene polysulfonated compounds. *iScience* **24**, 101952 (2021).
16. Wu, T. et al. Solar-driven efficient heterogeneous subminute water disinfection nanosystem assembled with fingerprint MoS_2. *Nat. Water* **1**, 462–470 (2023).
17. Daer, S., Goodwill, J. E. & Ikuma, K. Effect of ferrate and monochloramine disinfection on the physiological and transcriptomic response of *Escherichia coli* at late stationary phase. *Water Res.* **189**, 116580 (2021).
18. Zhu, Z. et al. Entropy of a bacterial stress response is a generalizable predictor for fitness and antibiotic sensitivity. *Nat. Commun.* **11**, 4365 (2020).
19. Lisle, J. T. et al. Effects of Starvation on Physiological Activity and Chlorine Disinfection Resistance in *Escherichia coli* O157:H7. *Appl. Environ. Microbiol.* **64**, 4658–4662 (1998).
20. Jiang, H. et al. Light-driven CO_2 methanation over Au-grafted $Ce_{0.95}Ru_{0.05}O_2$ solid-solution catalysts with activities approaching the thermodynamic limit. *Nat. Catal.* **6**, 519–530 (2023).
21. Jiang, J., Wang, X. & Guo, H. Enhanced Interfacial Charge Transfer/Separation By LSPR-Induced Defective Semiconductor Toward High Co_2 RR Performance. *Small* **19**, 2301280 (2023).
22. Cai, R. et al. Plasmonic AuPt@CuS Heterostructure with Enhanced Synergistic Efficacy for Radiophotothermal Therapy. *J. Am. Chem. Soc.* **143**, 16113–16127 (2021).
23. Xia, C. et al. General synthesis of single-atom catalysts with high metal loading using graphene quantum dots. *Nat. Chem.* **13**, 887–894 (2021).
24. Hai, X. et al. Scalable two-step annealing method for preparing ultra-high-density single-atom catalyst libraries. *Nat. Nanotechnol.* **17**, 174–181 (2022).
25. Sun, T. et al. Single-atomic cobalt sites embedded in hierarchically ordered porous nitrogen-doped carbon as a superior bifunctional electrocatalyst. *Proc. Natl. Acad. Sci.* **115**, 12692–12697 (2018).
26. Peugeot, A. et al. Benchmarking of oxygen evolution catalysts on porous nickel supports. *Joule* **5**, 1281–1300 (2021).
27. Cai, C., Sun, W., He, S., Zhang, Y. & Wang, X. Ceramic membrane fouling mechanisms and control for water treatment. *Front. Environ. Sci. Eng.* **17**, 126 (2023).
28. Zhao, C. et al. Solid-Diffusion Synthesis of Single-Atom Catalysts Directly from Bulk Metal for Efficient CO_2 Reduction. *Joule* **3**, 584–594 (2019).

29. Liang, Q. et al. Macroscopic 3D Porous Graphitic Carbon Nitride Monolith for Enhanced Photocatalytic Hydrogen Evolution. *Adv. Mater.* **27**, 4634–4639 (2015).
30. Zhu, L. et al. Designing 3D-MoS_2 Sponge as Excellent Cocatalysts in Advanced Oxidation Processes for Pollutant Control. *Angew. Chem. Int. Ed.* **59**, 13968–13976 (2020).
31. Jiang, Z. et al. Filling metal–organic framework mesopores with TiO_2 for CO_2 photoreduction. *Nature* **586**, 549–554 (2020).
32. Li, R., Chen, T. & Pan, X. Metal–Organic-Framework-Based Materials for Antimicrobial Applications. *ACS Nano* **15**, 3808–3848 (2021).
33. Zhang, X. et al. A General Method for Transition Metal Single Atoms Anchored on Honeycomb-Like Nitrogen-Doped Carbon Nanosheets. *Adv. Mater.* **32**, 1906905 (2020).
34. Yu, S. et al. Covalently bonded zeolitic imidazolate frameworks and polymers with enhanced compatibility in thin film nanocomposite membranes for gas separation. *J. Membr. Sci.* **540**, 155–164 (2017).
35. Ji, S. et al. Chemical Synthesis of Single Atomic Site Catalysts. *Chem. Rev.* **120**, 11900–11955 (2020).
36. You, J., Guo, Y., Guo, R. & Liu, X. A review of visible light-active photocatalysts for water disinfection: Features and prospects. *Chem. Eng. J.* **373**, 624–641 (2019).
37. Cao, S. et al. Single-Atom Engineering of Directional Charge Transfer Channels and Active Sites for Photocatalytic Hydrogen Evolution. *Adv. Funct. Mater.* **28**, 1802169 (2018).
38. Zhu, Z. et al. Construction of high-dispersed Ag/Fe_3O_4/g-C_3N_4 photocatalyst by selective photo-deposition and improved photocatalytic activity. *Appl. Catal. B Environ.* **182**, 115–122 (2016).
39. Wu, Z. et al. Dual-Site Activation Coupling with a Schottky Junction Boosts the Electrochemiluminescence of Carbon Nitride. *Angew. Chem. Int. Ed.* **62**, e202308257 (2023).
40. Zhang, W., Li, Y., Niu, J. & Chen, Y. Photogeneration of Reactive Oxygen Species on Uncoated Silver, Gold, Nickel, and Silicon Nanoparticles and Their Antibacterial Effects. *Langmuir* **29**, 4647–4651 (2013).
41. Abdi, J. Synthesis of Ag-doped ZIF-8 photocatalyst with excellent performance for dye degradation and antibacterial activity. *Colloids Surf. Physicochem. Eng. Asp.* **604**, 125330 (2020).
42. Guo, X., He, S., Meng, Z., Wang, Y. & Peng, Y. Ag@ZIF-8/g-C_3N_4 Z-scheme photocatalyst for the enhanced removal of multiple classes of antibiotics by integrated adsorption and photocatalytic degradation under visible light irradiation. *RSC Adv.* **12**, 17919–17931 (2022).
43. Li, P. et al. Metal-organic frameworks with photocatalytic bactericidal activity for integrated air cleaning. *Nat. Commun.* **10**, 2177 (2019).
44. Zhou, P., Luo, M. & Guo, S. Optimizing the semiconductor–metal-single-atom interaction for photocatalytic reactivity. *Nat. Rev. Chem.* **6**, 823–838 (2022).
45. Yang, L. et al. Cellular responses to reactive oxygen species are predicted from molecular mechanisms. *Proc. Natl. Acad. Sci.* **116**, 14368–14373 (2019).
46. Xia, D. et al. Single Ag atom engineered 3D-MnO_2 porous hollow microspheres for rapid photothermocatalytic inactivation of *E. coli* under solar light. *Appl. Catal. B Environ.* **245**, 177–189 (2019).
47. Nosaka, Y. & Nosaka, A. Y. Generation and Detection of Reactive Oxygen Species in Photocatalysis. *Chem. Rev.* **117**, 11302–11336 (2017).
48. Wang, W., Huang, G., Yu, J. C. & Wong, P. K. Advances in photocatalytic disinfection of bacteria: Development of photocatalysts and mechanisms. *J. Environ. Sci.* **34**, 232–247 (2015).
49. Li, W. et al. Ultrathin metal–organic framework membrane production by gel–vapour deposition. *Nat. Commun.* **8**, 406 (2017).
50. Wei, H. et al. Iced photochemical reduction to synthesize atomically dispersed metals by suppressing nanocrystal growth. *Nat. Commun.* **8**, 1490 (2017).
51. Fu, N. et al. Controllable Conversion of Platinum Nanoparticles to Single Atoms in Pt/CeO_2 by Laser Ablation for Efficient CO Oxidation. *J. Am. Chem. Soc.* **145**, 9540–9547 (2023).
52. Yang, C., Sun, W. & Ao, X. Bacterial inactivation, DNA damage, and faster ATP degradation induced by ultraviolet disinfection. *Front. Environ. Sci. Eng.* **14**, 13 (2020).
53. Yan, H., Song, X., Wang, X. & Wang, Y. Electromagnetic wave absorption and scattering analysis for Fe_3O_4 with different scales particles. *Chem. Phys. Lett.* **723**, 51–56 (2019).

Acknowledgements

This study was financially supported by the Beijing Natural Science Foundation (JQ24054, Y.L.), and the National Natural Science Foundation of China (grant numbers T2421005, X.H.X. and 52170024, Y.L.).

Author contributions

Y.L., W.Z. and J.W. conceived the idea and designed the research. J.W. conducted the experiments and performed the data analysis. J.Z. performed the electromagnetic simulation. Y.L., W.Z., J.-H.K., H.Y. and J.W. drafted the manuscript. J.W., Y.L. and X.X. reviewed and edited the manuscript.

Competing interests

The authors declare no competing interests.

Additional information

Supplementary information The online version contains supplementary material available at https://doi.org/10.1038/s41467-025-56339-2.

Correspondence and requests for materials should be addressed to Yang Li.

Peer review information *Nature Communications* thanks the anonymous, reviewers for their contribution to the peer review of this work. A peer review file is available.